Atomic-Scale Characterization of Negative Differential Resistance in Ferroelectric Bi2WO6

Chuangye Song, Huican Mao, Yuben Yang, Xin Liu, Zhiping Yin, Zhenpeng Hu, Kehui Wu, Jinxing Zhang

Atomic-Scale Characterization of Negative Differential Resistance in Ferroelectric Bi_2WO_6

Chuangye Song, Huican Mao, Yuben Yang, Xin Liu, Zhiping Yin, Zhenpeng Hu, Kehui Wu, and Jinxing Zhang**

Negative differential resistance (NDR), a quantum nonlinear electron transport process, has long attracted research interest owing to its intriguing underlying physics and promising applications in high-speed electronics. Here, the authors report the NDR behavior in (001)-oriented ferroelectric Bi_2WO_6 using scanning tunneling microscopy (STM). The current–voltage characteristics of the diode configuration consisting of an STM tip over the $[BiO]^+$-$[WO_4]^{2-}$-$[BiO]^+$ terrace exhibit NDR features. Scanning tunneling spectroscopy combined with density functional theory calculations indicates that the observed NDR results from robust resonant tunneling through confined energy levels within the 2D $[WO_4]^{2-}$ layer. The atomically resolved NDR found in such a transition metal oxide offers a unique band structure for novel ferroelectric-based devices.

1. Introduction

Negative differential resistance (NDR), which is a nonlinear electron transport phenomenon characterized by decreasing current with increasing voltage, has great potential for various electronic applications (e.g., fast switches,[1,2] oscillators,[3] and frequency-locking circuits[4]). In previous studies with scanning tunneling microscopy (STM), NDR has been attributed to resonant tunneling between localized narrow energy states on the STM tip and the specific surface sites.[5–7] Till date, NDR and the accompanying resonant tunneling behaviors have been studied mostly in conventional Si-based or III-V compound semiconductors,[8–13] organic molecules,[7,14] and graphene[9,15,16] using STM. However, a clear resonant tunneling behavior at the atomic scale has not been experimentally realized in strongly correlated transition metal oxides (TMOs), which may possess spatial electron confinement and peculiar quantum behaviors at reduced dimensions.[17–19]

Bi_2WO_6 (BWO) is a ferroelectric TMO with a layered-perovskite structure,[20,21] in which the $[WO_4]^{2-}$ layer is sandwiched between two $[Bi_2O_2]^{2+}$ layers, forming a natural 2D potential well.[22] The lowest unoccupied and highest occupied orbital levels are composed of the W-5*d* and O-2*p*/Bi-6*sp* hybrid orbitals, respectively.[23–25] Hania Djani et al. proposed that 2D electron gas could be confined in the perovskite $[WO_4]^{2-}$ layer via doping electrons occupied in the W-5*d* states around the bottom of the conduction band.[26] Wei et al. found that spontaneous spin polarization could be induced in the excited metastable BWO nanosheets,[27] where the photoexcited electrons are trapped in the $[WO_4]^{2-}$ layers and the photogenerated holes are trapped in the $[Bi_2O_2]^{2+}$ layers.[22] The unique potential well energy band and orbital occupancy in BWO motivated us to explore exotic phenomena and possible quantum transport behaviors.

Here, we report nonlinear electron tunneling transport observed in an atomically flat (001)-oriented $[BiO]^+$-$[WO_4]^{2-}$-$[BiO]^+$ terrace using low-temperature STM in ultrahigh vacuum. NDR can be observed under an appropriate negative voltage bias (V_b). A symmetric resonance exists at an opposite bias polarity, both of which can be remarkably enhanced by reducing the tip-sample distance. Furthermore, the NDR features disappear when the tip is moved to the symmetry-broken step edge, which is accompanied by a change in the scanning tunneling spectroscopy (STS) from hole type to electron type. Density functional theory (DFT) calculations further reveal electron confinement in the 2D $[WO_4]^{2-}$ layers.

2. Results and Discussion

BWO has a layered Aurivillius crystal structure with space group $Pca2_1$ and an orthorhombic lattice constant (a = 5.457 Å,

C. Song, H. Mao, Y. Yang, X. Liu, Z. Yin, J. Zhang
Department of Physics
Beijing Normal University
Beijing 100875, China
E-mail: jxzhang@bnu.edu.cn
C. Song, K. Wu
Songshan Lake Materials Laboratory
Dongguan, Guangdong 523808, China
E-mail: khwu@iphy.ac.cn
C. Song, H. Mao, K. Wu
Institute of Physics
Chinese Academy of Sciences
Beijing 100190, China
K. Wu
School of Physics
University of Chinese Academy of Sciences
Beijing 100049, China
Z. Hu
School of Physics
Nankai University
Tianjin 300071, China

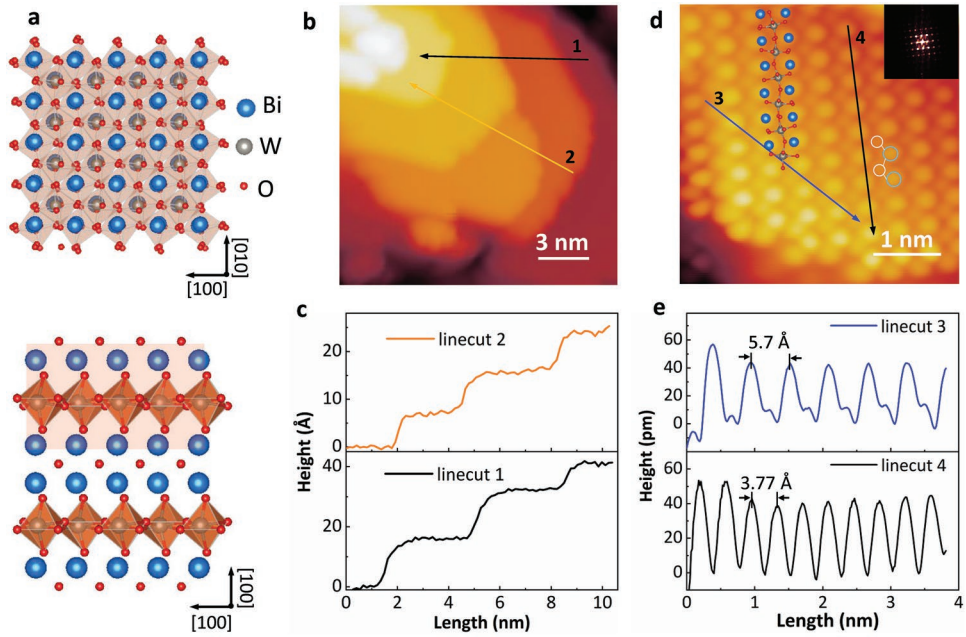

Figure 1. Topography of BWO surface imaged by STM. a) Top view (top panel) and side view (bottom panel) of the crystal structure of BWO. The $[BiO]^+$-$[WO_4]^{2-}$-$[BiO]^+$ sandwich substructure is marked by a light-red rectangle. b) Large-area STM image ($V_b = -2$ V, $I_t = 35$ pA) of the BWO surface shows a representative island growth mode. c) Height profile of steps along the orange and black arrows in (b). By comparing the step height with the c-axis crystal structure, the coexistence of one-half and one unit-cell height steps is determined. d) Atomically resolved STM image ($V_b = -2$ V, $I_t = 80$ pA). Both the surface layer ($[BiO]^+$) with larger corrugation and sublayer ($[WO_4]^{2-}$) with smaller corrugation are determined, and the detailed BWO ball-stick sketch is superimposed. White and cyan circles are used to highlight the sublayer tungsten and surface bismuth atoms, respectively. Inset is the corresponding fast Fourier transform (FFT) image. e) Line-cuts taken along the black and blue arrows in (d).

$b = 5.436$ Å, and $c = 16.427$ Å).[28] In this layered structure, the $[WO_4]^{2-}$ and the $[Bi_2O_2]^{2+}$ monolayers alternately stack together by means of strong chemical bonds, forming a naturally layered heterojunction, as shown in **Figure 1**a. The light-red rectangle marks the $[BiO]^+$-$[WO_4]^{2-}$-$[BiO]^+$ sandwich substructure with the height of a half-unit cell (≈0.82 nm). DFT calculations show that the surface energy of the sandwich configuration is 0.86 J m^{-2}, which is notably smaller than that of the non-sandwich substructure.[21] In our experiment, BWO thin films with a thickness of ≈10 nm were epitaxially grown on (001)-oriented Nb-doped $SrTiO_3$ (Nb-STO) substrates by pulsed laser deposition in an oxygen environment of 13 Pa. The laser energy was approximately 1 J cm^{-2} with a repetition rate of 1 Hz, and the substrate temperature was maintained at 700 °C during the film growth. Subsequently, the films were cooled to room temperature at 0.1 atm of oxygen at a cooling rate of 5 °C min^{-1}. Then, the BWO thin films were transferred in situ to the UHV-STM (UNISOKU USM 1500) with a base pressure of 6.0×10^{-11} Torr. The STM experiments were performed with Pt-Ir tips at 77 K in constant-current mode to obtain the STM images. A bias voltage (V_b) was applied to the samples.

Figure 1b shows a representative STM image, which reveals the island growth and the atomically flat terraces of the BWO thin film. The corresponding height profiles are shown in Figure 1c. Two different step heights, 0.82 and 1.64 nm, were identified experimentally, indicating the coexistence of half and one unit-cell steps at the (001)-oriented surface.[21] The high-resolution STM image in Figure 1d confirms the orthorhombic lattice structure of the (001)-oriented BWO, consisting of a large protrusion and a small protrusion in each unit cell. The nearest and second-nearest neighbors of the large protrusions are measured to be 3.77 and 5.47 Å in height by analyzing the line profiles (Figure 1e). These values are very close to the lattice constants of (001)-oriented BWO surface.[20] Based on the lowest surface energy of the $[BiO]^+$-$[WO_4]^{2-}$-$[BiO]^+$ sandwich substructure and our STM results, we attribute the large protrusions in STM images to bismuth (Bi) atoms, and the small protrusions to sublayer tungsten (W) atoms in each slab constituting a $[BiO]^+$-$[WO_4]^{2-}$-$[BiO]^+$ sandwich substructure. A ball-stick sketch of the surface $[BiO]^+$ layer and the $[WO_4]^{2-}$ sublayer is superimposed in Figure 1d, which is distinct from the reconstructed (113)-BWO films in our previous work.[29] It should be noted that such an unreconstructed, pristine (001)-oriented BWO surface has not been reported previously. The successful realization of high-quality (001)-oriented BWO thin films with alternately stacked $[BiO]^+$-$[WO_4]^{2-}$-$[BiO]^+$ layers provides a platform for exploring its exotic electronic structures and electron tunneling dynamics.

After the identification of the (001)-oriented BWO surface structure, we investigated the effect of the sample-tip distance (d_{st}) on the atomic symmetry in the STM images. As shown in **Figure 2**a, the square lattice of atomic-size protrusions from both the surface layer and sublayer can be resolved at a low tunneling current $I_t = 10$ pA. We acquired a series of STM images within the same area by changing only the I_t. Interestingly, we observed that two adjacent atoms selectively combine into a dimer-like structure at a higher $I_t = 500$ pA (Figure 2b). The line profiles (Figure 2c) along the arrows further reveal the change

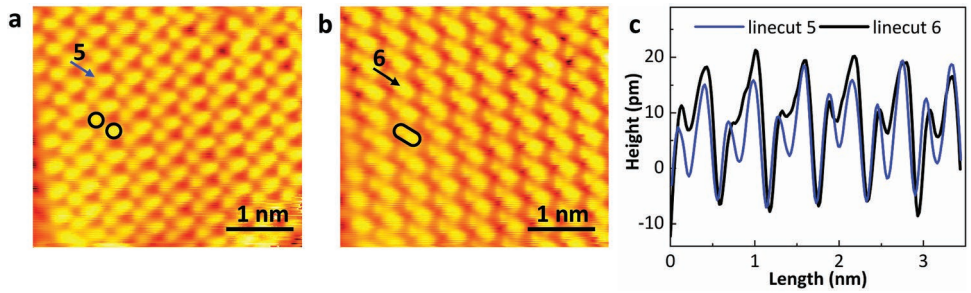

Figure 2. Tip-sample distance-dependent atomic structures of BWO surface. Consecutively acquired STM images with a) $I_t = 10$ pA and b) $I_t = 500$ pA, where $V_b = -1.5$ V. The scale bar is 1 nm. c) Linecuts recorded along the atomic arrays marked by blue and black arrows.

in the atomic geometry in the STM images before and after a change in I_t. With an increased tunneling current, the STM tip becomes closer to the sample,[30] that is, the d_{st} decreases. The d_{st}-dependent atomic imaging can be explained by a shift in the dominant electronic states during the tunneling process. Based on the partial density of states (PDOS) of the layered BWO slab,[31] the O-2*p*/Bi-6*p* in the surface [BiO]+ layer has a larger decay length in vacuum, and contributes the most to STM imaging with a larger d_{st}. The decay length of W-5*d* in the $[WO_4]^{2-}$ sublayer was relatively small. Consequently, STM imaging with a smaller d_{st} results from the mixed W-5*d* and O-2*p*/Bi-6*p* orbitals.

To explore the local electronic structure of the BWO surface, tunneling spectra measurements were performed. The tip position was maintained at a constant height, as determined by the feedback conditions. The sample voltage (V) was then swept from −2.5 to +1.5 V and the tunneling current (I) was recorded. Interestingly, we observed a remarkable difference in the I–V characteristics at the terrace and step edge, as shown in **Figure 3**a. The blue curve (#42) in the bottom panel taken at the step edge is relatively featureless, while the red curve (#1) taken directly on the terrace exhibits a clear NDR feature detected at negative V_b. The detailed I–V curves, as illustrated in Figure 3b, reveal the evolution of the I–V curves when the tip moves from the terrace toward the step edge. An apparent and smooth NDR behavior appears in the I–V curve at negative V_b on the terrace, with a maximum current (I_{max}) at −1.65 V and a minimum current (I_{min}) at −2.0 V, respectively. When the tip approaches the step edge, the overall current increases for both voltage polarities, resulting in a larger discrepancy with that on the terrace and the gradual disappearance of the NDR feature. Such a position-dependent increase in the current can be attributed to the largely enhanced electron density around the edge,[32] where the tunneling electrons from the partially exposed $[WO_4]^{2-}$ sublayers can be detected by the STM tip.[33] The corresponding differential tunneling conductance (dI/dV) curves, which are proportional to the local density of states (DOSs), are shown in Figure 3c. We observe two zero-crossing points around $V_b \approx -1.9$ V on the terrace and the damping of the NDR feature near the step edge. Interestingly, the evolution from a p-type (on the terrace) to an n-type (near step edge) band structure was identified (Figure 3d), which reveals the hole-type

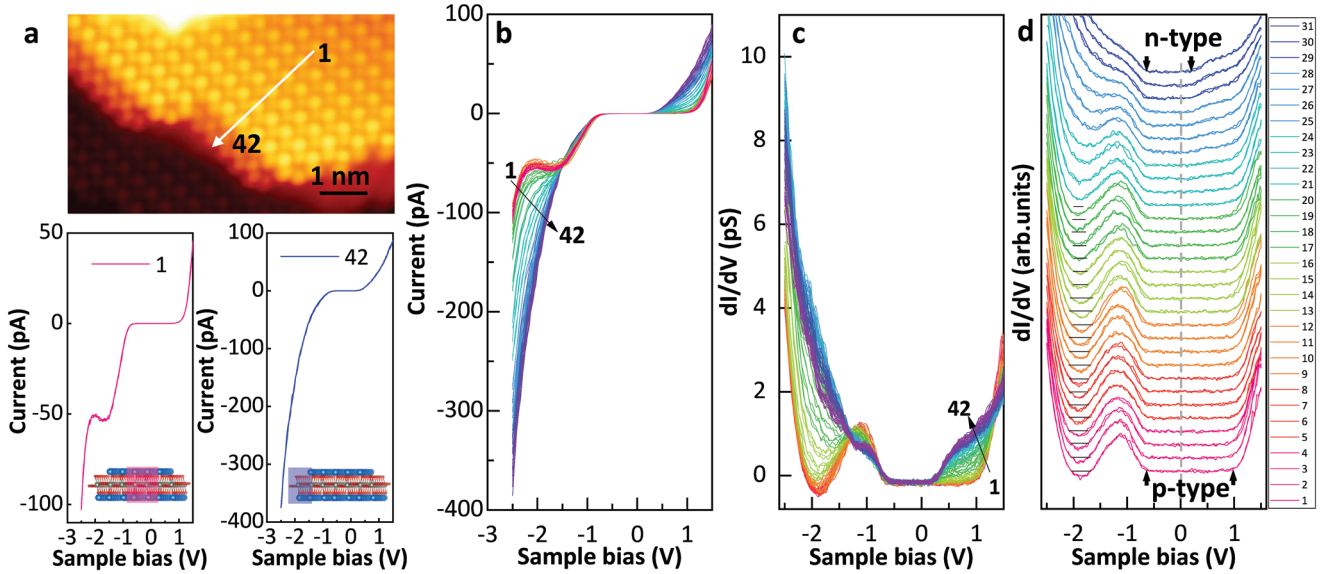

Figure 3. Electronic structures and NDR. a) Typical I–V curves with distinct features on the terrace and near the step edge. The STM image shows the location where the electron tunneling spectra are recorded. b) I–V curves ($V_b = -2$ V, $I_t = 50$ pA) measured with the Pt-Ir tip moving from the terrace (#1) towards the step edge (#42). c) Point dI/dV spectra ($V_{mod} = 5$ mV, $f_{mod} = 983$ Hz) taken at the same sites as the I–V curves in (b). d) The curves in (c) are shifted vertically for clarity.

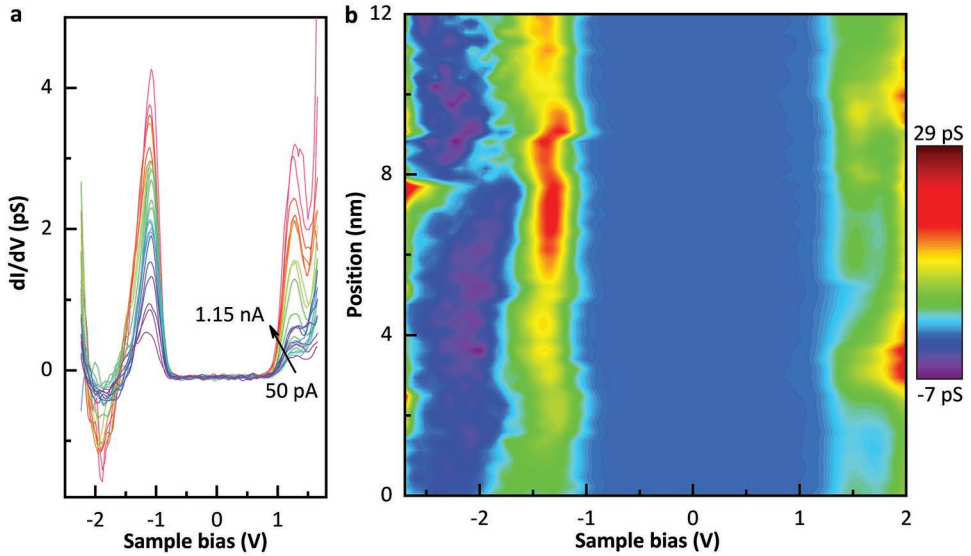

Figure 4. NDR as a function of tip-sample distance. a) dI/dV curves captured on the terrace with varied I_t = 50–1150 pA (50 pA interval), where V_b = –1.5 V. b) Site-dependent dI/dV curves recorded on the terrace. A uniform NDR feature is revealed in the figure.

nature of the $[BiO]^+$ layers and electron-type band structure of the $[WO_4]^{2-}$ layers.[22,27] The discrepancy in the bandgap between the surface (≈1.7 eV) and bulk (2.75 eV) is possibly due to the splitting of the O-2*p* states and the W-5*d* states at the top of the valence band and the bottom of the conduction band,[34] respectively. This difference can be explained by a simple perturbation of the crystal field when the symmetry is reduced.[35]

Furthermore, we performed STM measurements on ultrathin BWO films so that the tunneling electrons could be collected through the conductive Nb-STO substrate. As shown in Figure S1a–c, Supporting Information, half and one unit-cell BWO layers were grown on the Nb-STO. In contrast to the bare Nb-STO, the ultrathin BWO exhibited a typical NDR feature (see Figure S1d, Supporting Information). The dI/dV curve from the ultrathin BWO exhibits a larger peak width at half height, as well as a smaller bandgap, which may be attributed to the interfacial interactions or disordered perturbation at the interface with reduced symmetry.[36] With increasing BWO thickness, as shown in Figures S1e–f, Supporting Information, the occurrence of the NDR shifts to a lower sample voltage bias, accompanied by a larger bandgap, as revealed by the STS spectra. The stable NDR feature in the BWO surface with different thicknesses further indicates the strong electron confinement in the $[WO_4]^{2-}$ layer and the weak correlation between two neighboring $[BiO]^+$-$[WO_4]^{2-}$-$[BiO]^+$ sandwich substructures. Following the identification of the NDR on the BWO surface, we performed tunneling spectra measurements with varied tip-sample distances, as shown in **Figure 4**a. With the increase in I_t from 0.05 to 1.15 nA in the STS measurement, the distance between the tip and the sample is dramatically reduced, resulting in the creation of a stronger local electric field between the tip and the sample. The intensity of the NDR peak is dramatically enhanced, which implies that the coherent electron nonlinear transport between the tip apex and BWO surface is enhanced to some extent. In addition, corresponding to the NDR feature at negative sample bias, an almost symmetric resonance appears at a positive sample bias. The symmetric position of the energy level around the Fermi energy is similar to the behavior observed in quantum dots with quantized energy levels.[37,38] Furthermore, the tunneling spectra exhibited a uniform distribution of the NDR feature in real space, as shown in Figure 4b. Although the NDR behavior on the terrace was identified, the underlying physical mechanism needs to be further investigated.

To understand the origin of the NDR behavior, the DOSs of BWO and electron-doped BWO with different doping levels were calculated based on DFT. As shown in **Figure 5**a, the bottom of the conduction band in BWO is mainly dominated by W-5*d* and type III O-2*p* orbitals from the $[WO_4]^{2-}$ layer, and its lowest energy level is ≈1.0 eV lower than that of the Bi-6*p* and type II O-2*p* orbitals in the $[Bi_2O_2]^{2+}$ layer, leading to a natural potential well.[22] When the electron doping is increased (n = 0.1 e/u.c., 0.3 e/u.c., 0.5 e/u.c.), the bottom of the conduction band principally composed of W-5*d* and type III O-2*p* orbitals ($[WO_4]^{2-}$ layer) moves to a lower energy and crosses the Fermi level, making the BWO a conductor, as shown in Figures 5b–d. These orbitals in the $[WO_4]^{2-}$ layer make a major contribution to the electronic occupied states, which indicates that electron confinement mainly occurs in the $[WO_4]^{2-}$ layer. In heterostructures with sufficiently confined layers, quantum interference effects begin to appear prominently in the motion of the electrons, and the carrier densities become quantum mechanically degenerate (e.g., quantum well).[39–42] Quantized energy levels of carriers in the quantum well lead to a significant change in the electron transport,[43,44] for example, resonant tunneling between the quantized surface states and the STM tip could result in intriguing NDR behaviors.[45]

We performed electron transport simulations. For comparison, two types of tip models were used to simulate the STM I–V curves, including a pyramid-shaped cluster model[46] and a (111)-oriented slab model.[7] More details can be found in the DFT calculations. The calculated I–V curves from the two

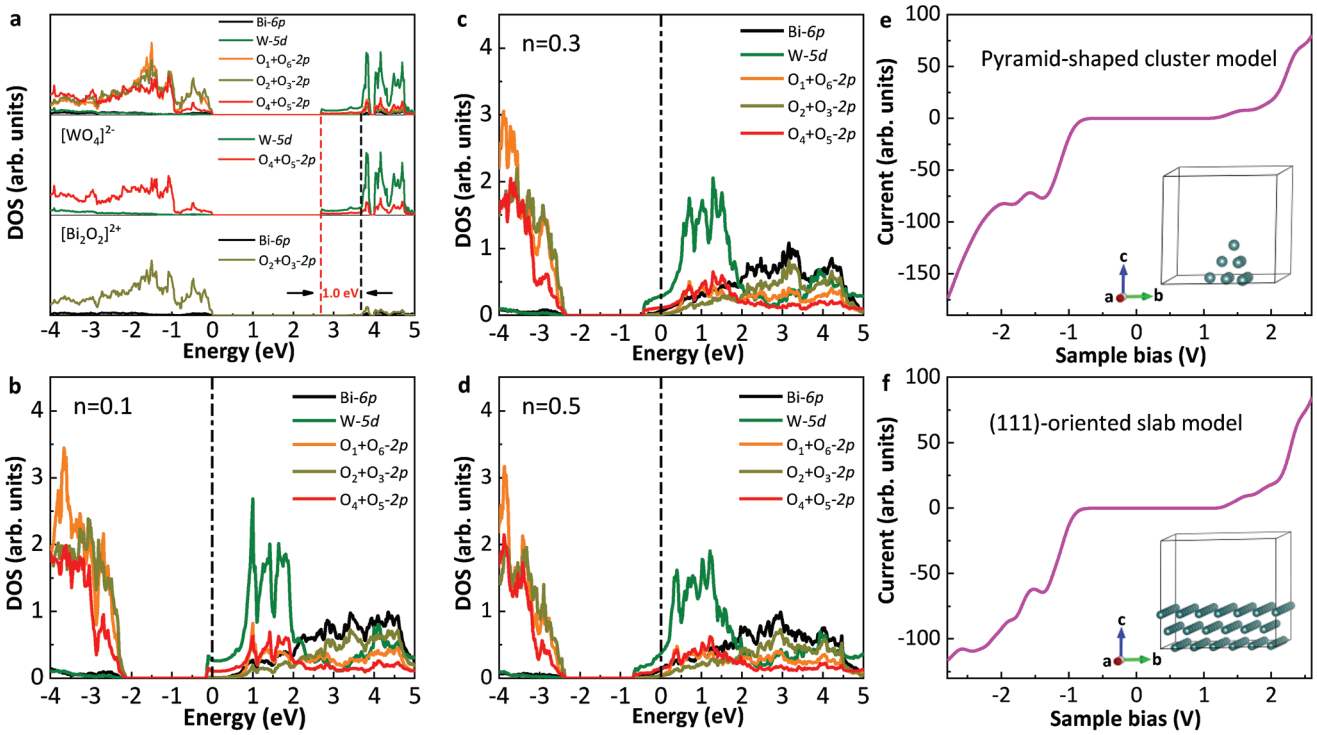

Figure 5. The DOSs of BWO. DOSs of electron-doped BWO with doping level n = (a) 0, (b) 0.1 e/u.c., c) 0.3 e/u.c., d) 0.5 e/u.c., respectively. In the layered BWO structure, the oxygen atoms are classified into three types depending on their chemical environments and hybridizations. Type-I oxygen atoms (O_1 and O_6) hybridize with both adjacent W and Bi atoms. Type-II oxygen atoms (O_2 and O_3) only hybridize with Bi atoms. Type-III oxygen atoms (O_4 and O_5) only hybridize with W atoms. The bottom of the conduction band, which is dominated by W-5*d* and type III O-2*p* orbitals from $[WO_4]^{2-}$ layer, moves to a lower energy level and crosses the Fermi level when the electron doping level is increased, which indicates that the electrons are principally confined in the $[WO_4]^{2-}$ layers. The simulated STM *I*–*V* curves obtained from pyramid-shaped cluster model in (e) and from (111)-oriented slab model in (f). The insets are the tips models, and u.c. represents unit cell.

models exhibit similar NDR behavior, as shown in Figures 5e–f. I_{max} appears at –1.4 V (–1.4 V) and I_{min} at –1.6 V (–1.55 V) in Figure 5e (Figure 5f). These results are in approximate agreement with the experimental results obtained within the instrument resolution in this work, which further indicates that the NDR behavior in $[BiO]^+$-$[WO_4]^{2-}$-$[BiO]^+$ sandwich substructure shows no dependence on the geometrical shape of the tip. Furthermore, we also observed additional weaker NDR-like behaviors, such as the occurrence of I_{max} and I_{min} near –1.8 V in Figure 5e and near –2.4 V in Figure 5f, respectively, which are possibly attributed to the discrete quantized energy levels in this sandwich substructure. However, considering the instrument energy resolution, signal-to-noise ratio, etc., additional weaker NDR-like behaviors are absent in the STM *I*–*V* curves.

Thus, we propose that the NDR is a result of resonant tunneling through the confined energy levels in the subsurface $[WO_4]^{2-}$ layer (see the schematic illustrated in **Figure 6**b). The quantized states in the potential well, as shown in Figure 6c, are similar to the quantum well in conventional semiconductors.[40,47,48] Figures 6d–f schematically summarize the electron tunneling mechanism with energy band diagrams. Figure 6d shows equilibrium band diagrams for the adjacent $[WO_4]^{2-}$ and $[BiO]^+$ surface layers, where the Fermi level (E_F) aligns and is within the conduction band due to electron confinement in the $[WO_4]^{2-}$ sublayer. Figure 6e illustrates the case in which a negative bias is applied to the sample with respect to the grounded Pt-Ir tip. At a critical V_b, the E_F is lifted, and the electrons begin to selectively occupy the empty quantized energy level near the bottom of the $[WO_4]^{2-}$ conduction band, while the continuum conduction band of the adjacent $[BiO]^+$ is maintained. Consequently, this narrow-occupied energy band in the $[WO_4]^{2-}$ sublayer resulted in a sharp increase in the tunneling current. As V_b is increased to a slightly higher value, the narrow energy band moves off the E_F, and the corresponding tunneling current gradually decreases, forming an NDR feature in the *I*–*V* curves. Figure 6f depicts the situation for the opposite polarity. In this case, the E_F of BWO will drop across the continuum valence band edge, which is dominated by Bi-6*p* and O-2*p* orbitals, and electrons from the tip can tunnel into the continuum energy. However, owing to the existence of a quantized energy level in the $[WO_4]^{2-}$ layer, the tunneling current can be enhanced when the E_F passes through an individual quantum level, which results in an almost symmetric differential conductance peak, as shown in Figure 4a.

3. Conclusion

NDR behavior is directly observed with an atomic resolution in a layered ferroelectric BWO using STM/STS. We attribute this NDR feature to resonant tunneling through local confined

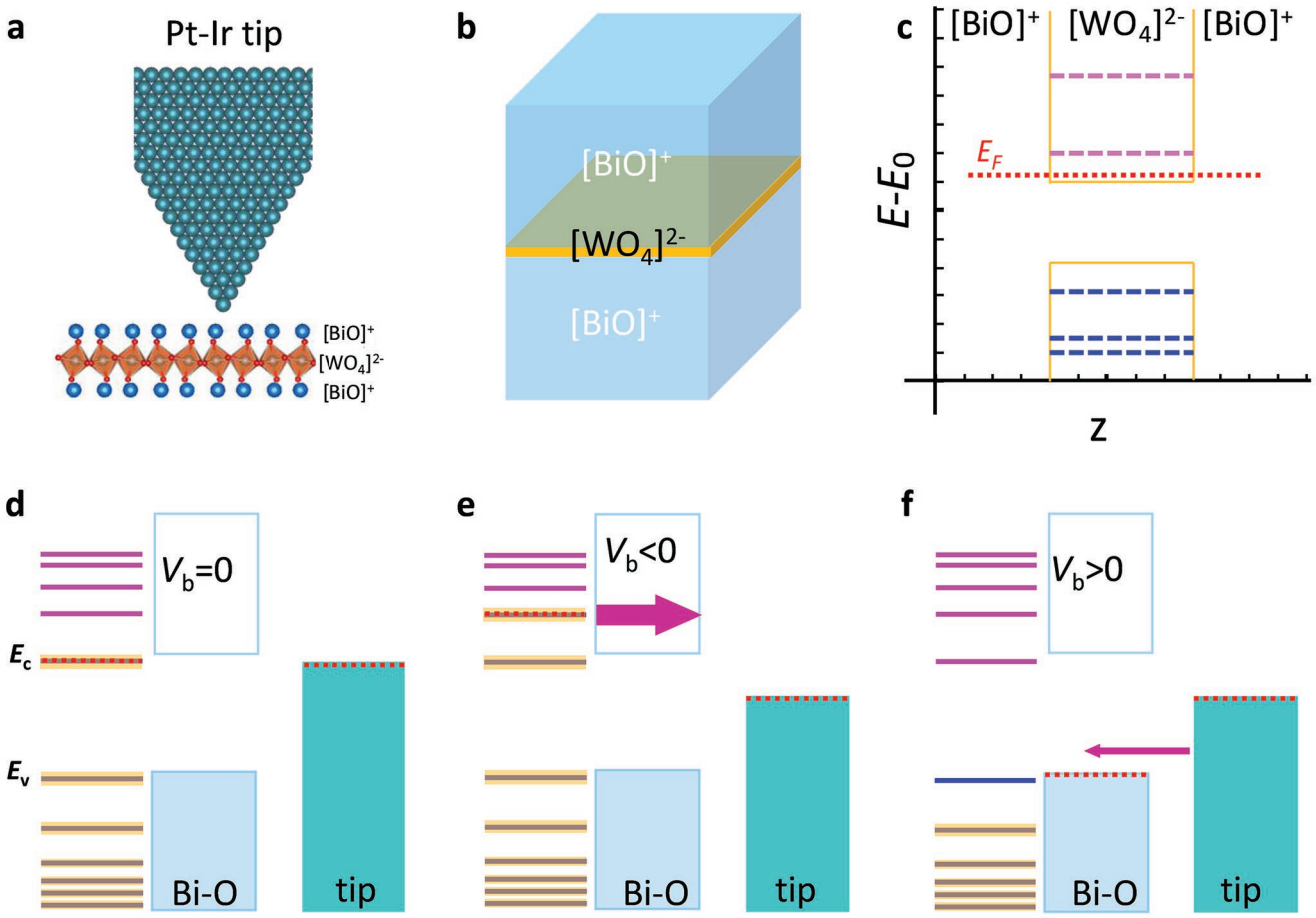

Figure 6. Quantum well states in the $[BiO]^+$-$[WO_4]^{2-}$-$[BiO]^+$ sandwich substructure. a) Schematic of the STM setup on $[BiO]^+$-$[WO_4]^{2-}$-$[BiO]^+$ sandwich substructure. b) Schematic illustrating $[WO_4]^{2-}$ layer (small bandgap) confined between two $[BiO]^+$ layers (large bandgap) in BWO. c) $[BiO]^+$-$[WO_4]^{2-}$-$[BiO]^+$ quantum well band diagram. E_F shows the quasi-Fermi level, where the pink and blue lines are the indices for the conduction and valence sub-bands, respectively. Note that only the first two/three conduction/valence sub-band edges are shown. d–f) Schematic band diagrams: d) Equilibrium, where the Fermi level aligns and is within the conduction band due to electron confinement in $[WO_4]^{2-}$ layer. e) NDR resonance, where the chemical potential shifts the band of electrons into the discrete energy levels in the conduction band with $V_b < 0$. f) The chemical potential shifts downwards with $V_b > 0$. Here, the discrete level falls within the continuum band of the $[BiO]^+$layer, and the resonance weakens.

energy levels in the $[WO_4]^{2-}$ layer, which implies the existence of an intrinsic quantum well. The highly reproducible NDR behavior in the proposed ferroelectric not only demonstrates quantum well band structures in TMOs but may also provide insights for designing novel ferroelectric-based devices.

4. Experimental Section

DFT Calculations: The DOSs calculations were performed using the full-potential linearized augmented plane wave method, as implemented in the WIEN2k package.[49] We used the Perdew–Burke–Ernzerhof (PBE) exchange-correlation potential[50] for structure relaxation, and further used the modified Becke–Johnson (mBJ) exchange potential[51] to calculate the electronic structure of bulk BWO in order to accurately predict the experimental bandgap. In the calculations, the muffin-tin radii were kept at 2.04, 1.79, 1.59 Bohr radius for Bi, W, O respectively, and the $R_{mt}K_{max}$ was fixed at 7.0. We adopted a bulk BWO structure with experimental lattice constants (a = 5.457 Å, b = 5.436 Å, and c = 16.427 Å, $P2_1ab$ space group).[52] In the structure relaxation, we relaxed the atomic positions, keeping the lattice constants fixed. In this layered structure, the oxygen atoms of BWO can be classified into three types depending on their hybridizations and chemical environments. The type-I oxygen atoms (O_1 and O_6) hybridize with both the adjacent W and Bi atoms. The type-II oxygen atoms (O_2 and O_3) hybridize only with Bi atoms, whereas the type-III oxygen atoms (O_4 and O_5) hybridize only with W atoms. To study the electron doping effect, the DOSs of electron-doped BWO with doping electrons n = 0.1, 0.3, 0.5 e/u.c. were calculated based on the ab-initio virtual crystal approximation (VCA) method in WIEN2K with PBE exchange-correlation potential.

Our previous DFT calculations of BWO show that there is almost no difference between the calculation results from the WIEN2K and VASP packages.[22] Thus, the STM I–V curves were simulated using the VASP package[53] with the PBE exchange-correlation potential.[50] As the proportion of Ir in the Pt-Ir tip is small (≤5%), we used Pt metal to construct the tip models. For the tips, we used two kinds of tip models, a pyramid-shaped cluster model (similar to the one used in reference,[46] the inset in Figure 5e) and a (111)-oriented slab model consisting of a (3 × 3) supercell with three atom layers in the ab-plane and a 10 Å vacuum layer along the c direction (similar to the one used in reference,[7] the inset in Figure 5f). In the structure relaxation, we relaxed ions and changed the cell shape and cell volume for bulk Pt metal and BWO, whereas only the atomic positions were relaxed for the two types of tip models. An energy cutoff of 400 eV (Pt-tip) and 550 eV (BWO) and an energy and force convergence criterion of

10^{-6} eV and 0.01 eV Å^{-1}, respectively, were employed. We simulated the STM *I–V* curves using the Fermi golden rule with the modified Bardeen approximation:[7]

$$I = \frac{8\pi^2 e}{h} \int_{E_F}^{E_F+eV} \rho_s(E)\,\rho_t(E-eV)\left|M_{st}\right|^2 dE \quad (1)$$

where E_F is the Fermi energy, ρ is the DOSs, and the indices *s* and *t* represent the tip and the sample, respectively. M_{st} is the tunneling matrix element between the tip and sample states. For simplicity, we set M_{st} as 1.

Acknowledgements

C.S. and H.M. contributed equally to this work. This work was supported by the National Key Research and Development Program of China (Grants No. 2016YFA0302300, 2017YFA0303304), the National Natural Science Foundation of China (Grants No. 11974052, 21873015, 11825405), the Strategic Priority Research Program of the Chinese Academy of Sciences (Grant No. XDB30103000), the Guangdong Basic and Applied Basic Research Foundation (Grant No. 2021A1515010030), and the China Postdoctoral Science Foundation (Grant No. 2020M670502).

Conflict of Interest

The authors declare no conflict of interest.

[1] C. P. Collier, G. Mattersteig, E. W. Wong, Y. Luo, K. Beverly, J. Sampaio, F. M. Raymo, J. F. Stoddart, J. R. Heath, *Science* **2000**, *289*, 1172.

[2] G. K. Ramachandran, T. J. Hopson, A. M. Rawlett, L. A. Nagahara, A. Primak, S. M. Lindsay, *Science* **2003**, *300*, 1413.

[3] E. R. Brown, J. R. Söderström, C. D. Parker, L. J. Mahoney, K. M. Molvar, T. C. McGill, *Appl. Phys. Lett.* **1991**, *58*, 2291.

[4] E. G. Gwinn, R. M. Westervelt, *Phys. Rev. Lett.* **1986**, *57*, 1060.

[5] P. Bedrossian, D. M. Chen, K. Mortensen, J. A. Golovchenko, *Nature* **1989**, *342*, 258.

[6] I.-W. Lyo, P. Avouris, *Science* **1989**, *245*, 1369.

[7] L. Chen, Z. Hu, A. Zhao, B. Wang, Y. Luo, J. Yang, J. G. Hou, *Phys. Rev. Lett.* **2007**, *99*, 146803.

[8] N. P. Guisinger, M. E. Greene, R. Basu, A. S. Baluch, M. C. Hersam, *Nano Lett.* **2004**, *4*, 55.

[9] X. Zheng, W. Lu, T. A. Abtew, V. Meunier, J. Bernholc, *ACS Nano* **2010**, *4*, 7205.

[10] N. P. Guisinger, N. L. Yoder, M. C. Hersam, *Proc. Natl. Acad. Sci. U. S. A.* **2005**, *102*, 8838.

[11] M. Berthe, R. Stiufiuc, B. Grandidier, D. Deresmes, C. Delerue, D. Stiévenard, *Science* **2008**, *319*, 436.

[12] I. H. Hong, T. M. Chen, Y. F. Tsai, *Appl. Phys. Lett.* **2012**, *101*, 053113.

[13] L. Esaki, *Phys. Rev.* **1958**, *109*, 603.

[14] S. Y. Quek, J. B. Neaton, M. S. Hybertsen, E. Kaxiras, S. G. Louie, *Phys. Rev. Lett.* **2007**, *98*, 066807.

[15] S.-Y. Li, H. Liu, J.-B. Qiao, H. Jiang, L. He, *Phys. Rev. B* **2018**, *97*, 115442.

[16] K. S. Kim, T. H. Kim, A. L. Walter, T. Seyller, H. W. Yeom, E. Rotenberg, A. Bostwick, *Phys. Rev. Lett.* **2013**, *110*, 036804.

[17] A. Ohtomo, H. Y. Hwang, *Nature* **2004**, *427*, 423.

[18] S. Samanta, S. B. Mishra, B. R. K. Nanda, *Phys. Rev. B* **2018**, *98*, 115155.

[19] H. Zhang, Y. Yun, X. Zhang, H. Zhang, Y. Ma, X. Yan, F. Wang, G. Li, R. Li, T. Khan, Y. Chen, W. Liu, F. Hu, B. Liu, B. Shen, W. Han, J. Sun, *Phys. Rev. Lett.* **2018**, *121*, 116803.

[20] C. Wang, X. Ke, J. Wang, R. Liang, Z. Luo, Y. Tian, D. Yi, Q. Zhang, J. Wang, X. F. Han, G. Van Tendeloo, L. Q. Chen, C. W. Nan, R. Ramesh, J. Zhang, *Nat. Commun.* **2016**, *7*, 10636.

[21] Y. Zhou, Y. Zhang, M. Lin, J. Long, Z. Zhang, H. Lin, J. C. Wu, X. Wang, *Nat. Commun.* **2015**, *6*, 8340.

[22] Y. Yang, H. Mao, J. Wang, Q. Zhang, L. Jin, C. Wang, Y. Zhang, N. Su, F. Meng, Y. Yang, R. Xia, R. Chen, H. Zhu, L. Gu, Z. Yin, C. W. Nan, J. Zhang, *Adv. Mater.* **2020**, *32*, 2003033.

[23] H. Fu, C. Pan, W. Yao, Y. Zhu, *J. Phys. Chem. B* **2005**, *109*, 22432.

[24] G. Zhang, Z. Hu, M. Sun, Y. Liu, L. Liu, H. Liu, C.-P. Huang, J. Qu, J. Li, *Adv. Funct. Mater.* **2015**, *25*, 3726.

[25] F. Ren, J. Zhang, Y. Wang, *RSC Adv.* **2015**, *5*, 29058.

[26] H. Djani, A. C. Garcia-Castro, W.-Y. Tong, P. Barone, E. Bousquet, S. Picozzi, P. Ghosez, *npj Quantum Mater.* **2019**, *4*, 51.

[27] J. Wei, Y. Xia, A. Qayum, X. Jiao, D. Chen, T. Wang, *Small* **2020**, *16*, 2005704.

[28] Y. Yoneda, S. Kohara, H. Takeda, T. Tsurumi, *Jpn. J. Appl. Phys.* **2012**, *51*, 09LE06.

[29] C. Song, J. Gao, J. Liu, Y. Yang, C. Tian, J. Hong, H. Weng, J. Zhang, *ACS Appl. Mater. Interfaces* **2020**, *12*, 4150.

[30] Y. Takahashi, T. Miyamachi, K. Ienaga, N. Kawamura, A. Ernst, F. Komori, *Phys. Rev. Lett.* **2016**, *116*, 056802.

[31] M. Li, Y. Dai, W. Wei, B. Huang, *Phys. Chem. Chem. Phys.* **2018**, *20*, 9221.

[32] F. Reis, G. Li, L. Dudy, M. Bauernfeind, S. Glass, W. Hanke, R. Thomale, J. Schäfer, R. Claessen, *Science* **2017**, *357*, 287.

[33] Z. Alpichshev, J. G. Analytis, J. H. Chu, I. R. Fisher, A. Kapitulnik, *Phys. Rev. B* **2011**, *84*, 041104(R).

[34] F. Wang, C. Di Valentin, G. Pacchioni, *ChemCatChem* **2012**, *4*, 476.

[35] O. Bengone, M. Alouani, J. Hugel, P. Blöchl, *Comput. Mater. Sci.* **2002**, *24*, 192.

[36] R. F. Berger, C. J. Fennie, J. B. Neaton, *Phys. Rev. Lett.* **2011**, *107*, 146804.

[37] U. Banin, Y. Cao, D. Katz, O. Millo, *Nature* **1999**, *400*, 542.

[38] O. Millo, D. Katz, Y. Cao, U. Banin, *Phys. Rev. B* **2000**, *61*, 16773.

[39] K. Yoshimatsu, K. Horiba, H. Kumigashira, T. Yoshida, A. Fujimori, M. Oshima, *Science* **2011**, *333*, 319.
[40] H. Fang, H. A. Bechtel, E. Plis, M. C. Martin, S. Krishna, E. Yablonovitch, A. Javey, *Proc. Natl. Acad. Sci. U. S. A.* **2013**, *110*, 11688.
[41] I. Matsuda, T. Ohta, H. W. Yeom, *Phys. Rev. B* **2002**, *65*, 085327.
[42] R. K. Kawakami, E. Rotenberg, H. J. Choi, E. J. Escorcia-Aparicio, M. O. Bowen, J. H. Wolfe, E. Arenholz, Z. D. Zhang, N. V. Smith, Z. Q. Qiu, *Nature* **1999**, *398*, 132.
[43] M. Schackert, T. Markl, J. Jandke, M. Holzer, S. Ostanin, E. K. Gross, A. Ernst, W. Wulfhekel, *Phys. Rev. Lett.* **2015**, *114*, 047002.
[44] C. Mittag, M. Karalic, Z. Lei, C. Thomas, A. Tuaz, A. T. Hatke, G. C. Gardner, M. J. Manfra, T. Ihn, K. Ensslin, *Phys. Rev. B* **2019**, *100*, 075422.
[45] J.-Y. Cheng, B. L. Fisher, N. P. Guisinger, C. M. Lilley, *npj Quantum Mater.* **2017**, *2*, 25.
[46] X. Q. Shi, W. W. Pai, X. D. Xiao, J. I. Cerdá, R. Q. Zhang, C. Minot, M. A. Van Hove, *Phys. Rev. B* **2009**, *80*, 075403.
[47] R. Chaudhuri, S. J. Bader, Z. Chen, D. A. Muller, H. G. Xing, D. Jena, *Science* **2019**, *365*, 1454.
[48] M. A. Khan, J. N. Kuznia, J. M. Van Hove, N. Pan, J. Carter, *Appl. Phys. Lett.* **1992**, *60*, 3027.
[49] P. Blaha, K. Schwarz, G. K. H. Madsen, D. Kvasnicka, J. Luitz, K. Schwarz, *WIEN2k, An Augmented Plane Wave and Local Orbitals Program for Calculating Crystal Properties* (Ed: K. Schwartz), Technical Universität Wien, Austria **2001**.
[50] J. P. Perdew, K. Burke, M. Ernzerhof, *Phys. Rev. Lett.* **1996**, *77*, 3865.
[51] F. Tran, P. Blaha, *Phys. Rev. Lett.* **2009**, *102*, 226401.
[52] H. Djani, P. Hermet, P. Ghosez, *J. Phys. Chem. C* **2014**, *118*, 13514.
[53] G. Kresse, J. Furthmüller, *Comput. Mater. Sci.* **1996**, *6*, 15.

Supplementary Materials for

Atomic-Scale Characterization of Negative Differential Resistance in Ferroelectric Bi_2WO_6

Chuangye Song,[1,2,3‡] Huican Mao,[1,3‡] Yuben Yang,[1] Xin Liu,[1] Zhipin Yin,[1] Zhenpeng Hu,[5] Kehui Wu[2,3,4*] and Jinxing Zhang[1*]

[1]Department of Physics, Beijing Normal University, Beijing 100875, China

[2]Songshan Lake Materials Laboratory, Dongguan, Guangdong 523808, China

[3]Institute of Physics, Chinese Academy of Sciences, Beijing 100190, China

[4]School of Physics, University of Chinese Academy of Sciences, Beijing 100049, China

[5]School of Physics, Nankai University, Tianjin 300071, China.

Corresponding authors: khwu@iphy.ac.cn; jxzhang@bnu.edu.cn;

[‡]These authors contributed equally to this work.

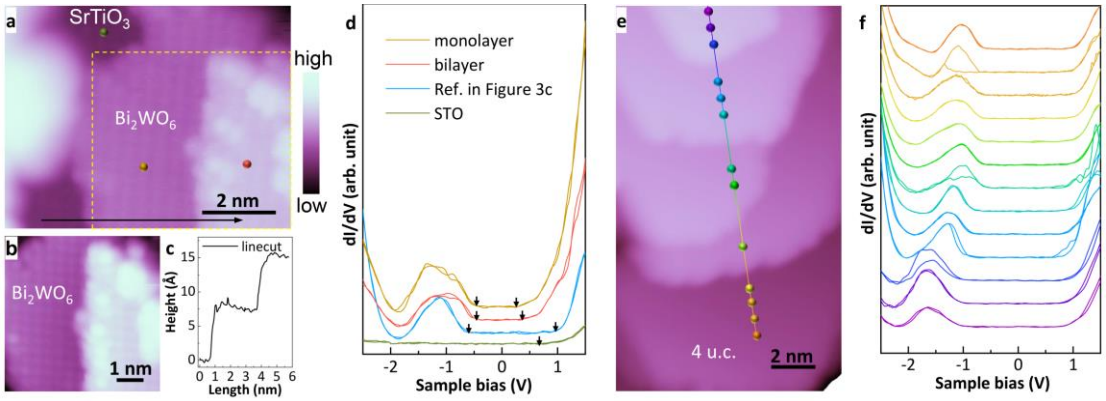

Figure S1. (a) STM image (V_b = -1.5 V, I_t = 100 pA) of BWO ultrathin film grown on Nb-STO (001). (b) Atomically resolved zoom-in scan of the yellow rectangle in (a). (c) Line profiles along the black arrow in (a), confirming the step with half-unit cell in height. (d) Typical dI/dV spectra measured on the monolayer, bilayer, and Nb-STO substrate. The dI/dV curve in Figure 3c is used as a reference; the locations where the dI/dV curves were obtained are marked with colored spheres in (a). (e) Topographic images (V_b = -2 V, I_t = 35 pA) of few-layer BWO thin film. (f) dI/dV curves obtained at the locations marked in (e).